Synthetic *Spitzer* Infrared Array Camera band maps from simulations of protostellar jets

Michael D. Smith[1]⋆ and Alexander Rosen[2]⋆

[1]*Armagh Observatory, College Hill, Armagh BT61 9DG*
[2]*Dublin City University, School of Mathematics, Glasnevin, Dublin 9, Ireland*

ABSTRACT

The bandpasses for *Spitzer* images contain numerous molecular hydrogen emission lines. With the additional complication of the non-uniform spectral response, it is necessary to calculate model images in order to analyse observations of molecular outflows. We employ three-dimensional hydrodynamic simulations of a range of dense supersonic molecular jets, including various degrees of velocity pulsation and precession, to demonstrate how the observed structure depends on the band. Features in band 1, which is dominated by emission from vibrational levels, are even more concentrated than in *K*-band images. In contrast, bands 2–4 are dominated by rotational lines and bow shock wings appear extended. Especially in band 4, broken cavity walls can be detectable. An initial comparison with *Spitzer* data is made.

Key words: hydrodynamics – shock waves – ISM: clouds – ISM: jets and outflows – ISM: molecules.

1 INTRODUCTION

Protostars drive powerful and spectacular outflows. They are collimated to various degrees and often extend to parsecs from the launching protostar (Richer et al. 2000; Reipurth & Bally 2001; McGroarty, Ray & Bally 2004). In our quest to understand their origin and environment, they have been imaged at many wavelengths from the optical to the millimetre. In particular, near-infrared and optical imaging have revealed that many of the outflows from the youngest protostars are formed via jets of molecular gas. Now, the *Spitzer* satellite has opened up a new part of the spectrum in which outflows can be spatially resolved. Here, we present synthetic observations in the infrared, derived from hydrodynamic simulations of jet-driven outflows, in order to deliver a means of understanding the global properties.

Near-infrared observations have proven especially useful because (i) strong emission originates from molecular hydrogen gas heated above 1000 K and (ii) the emission is not obscured by dust extinction except close to the protostar. Images in the 1–0 S(1) line, in the middle of the *K* band at 2.12 µm, are commonly acquired, displaying bow shocks and diverse other shock features (Davis 2002). Further into the infrared, there are numerous other H_2 lines which, as the *Infrared Space Observatory* (*ISO*) confirmed, are strong channels for radiation from gas at temperatures 300–800 K (e.g. Smith, Eisloffel & Davis 1998). Although there is plenty of cool gas, with a resolution of 14–27 arcsec in the mid-infrared, the *ISO* could not identify even the global structure of the outflow. In comparison, the Infrared

Array Camera (IRAC) instrument on board *Spitzer* has a pixel size of 1.2 arcsec and will thus soon yield the infrared structure of many outflows in some detail.

Unfortunately, the IRAC images are not straightforward to interpret for three reasons (Noriega-Crespo et al. 2004a). First, the four bands contain the wavelengths of many H_2 lines originating from several vibrational levels widely spaced in energy (Fig. 1). Secondly, the spectral response is a quite sensitive function of the wavelength within the band. Thirdly, atomic lines, polycyclic aromatic hydrocarbon features, dust grain emission and CO vibrational bands may all contribute. As a consequence, the individual contributions of each H_2 line cannot be extracted and the physical conditions of the gas cannot be ascertained. Nevertheless, lower excitation lines are generally expected to be more prominent at longer wavelengths in the mid-infrared, providing the basis for a qualitative interpretation (Noriega-Crespo et al. 2004a).

In this paper, we focus on the H_2 emission and consider predictions for outflows and outflow regions where these lines might dominate. Under the above circumstances, the remaining means of progress are (i) to calculate the emission properties from each potential model, (ii) to determine the major differences between between model predictions and observations and so (iii) to suggest a new model which should better accommodate the data. In response, to aid upcoming observations, we present here the predicted fluxes and images from a range of hydrodynamic simulations based on a physical model and numerical technique, which provide the most fundamental starting point.

The two motivating questions here are as follows. What differences in H_2 structure and fluxes are predicted between bands and between the near-infrared and the bands? How much might these
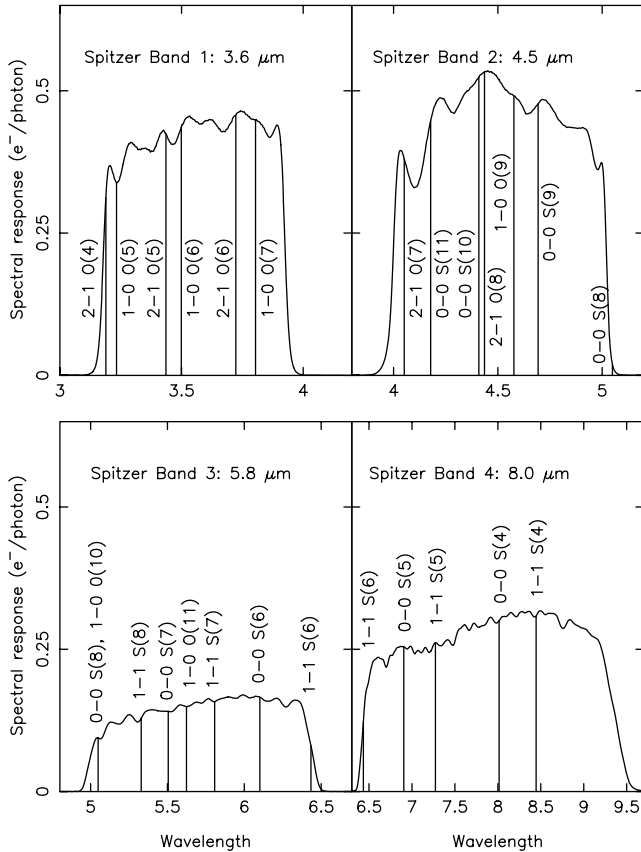
⋆E-mail: mds@arm.ac.uk (MDS); alex.rosen@dcu.ie (AR)

Figure 1. The spectral response functions for the four *Spitzer* IRAC bands and the spectral locations of the many contributing molecular hydrogen lines. Fluxes are derived in the simulations for each pixel and for each line and then multiplied by the spectral response before summing up to yield the band flux.

trends be dependent on the assumed physics? We will also provide a very brief comparison with the first published images.

2 MOLECULAR HYDROGEN LINES IN THE *SPITZER* BANDS

Important contributing H_2 lines and spectral response functions are displayed in Fig. 1. To help determine which lines to include in the development of our synthetic images, we first considered steady-state planar and curved shock models. A comparison was made with Cepheus E (Cep E), as it was observed with *Spitzer* (Noriega-Crespo et al. 2004b) and the *K*-band lines have been modelled in detail (Smith, Froebrich & Eislöffel 2003). A list of the brightest lines predicted for Cep E from both magnetohydrodynamic shocks (J-type radiative) and shocks with ambipolar diffusion (C-type) are provided in Table 1.

The best fits to the near-infrared emission were found to arise from bow-shaped shocks. The relative line fluxes are sensitive to the exact shape of the bow. Thus, the *K*-band fluxes predetermine the bow shock configuration. For this reason, the table indicates that the predicted H_2 fluxes in IRAC bands for steady-state C-shock (in which the process of ambipolar diffusion causes the magnetic field to slip through the neutral gas while the ions gradually transfer momentum between the two) are not so different from a J-shock model (the C-type bow shock emits somewhat less in lines originating from both the very highest and very lowest upper energy levels).

Table 1. The relative luminosities of H_2 lines in the IRAC bands derived from models for steady bow shock waves previously found to interpret Cep E South in the near-infrared. Luminosities are relative to the 1–0 S(1) luminosity of 0.33 $L_\odot$, as given in table 5 of Smith et al. (2003). *T* (K) is the energy/k of the upper level of the transition in kelvin. Note that the 1–0 O(5) line originates from the same upper energy level as the 1–0 S(1) line.

Line	T (K)	Wavelength (μ)	Bow J	Bow C
1–0 O(4)	6471	3.003	0.196	0.194
1–0 O(5)	6956	3.234	0.394	0.394
2–1 O(5)	12550	3.437	0.036	0.031
1–0 O(6)	7586	3.500	0.074	0.074
0–0 S(14)	19400	3.724	0.044	0.029
1–0 O(7)	8365	3.806	0.112	0.112
0–0 S(13)	17449	3.845	0.162	0.114
0–0 S(12)	15547	3.996	0.065	0.049
0–0 S(11)	13707	4.180	0.236	0.191
0–0 S(10)	11946	4.409	0.094	0.082
1–1 S(11)	18980	4.416	0.043	0.029
0–0 S(9)	10265	4.693	0.342	0.321
1–1 S(9)	15722	4.953	0.041	0.030
0–0 S(8)	8682	5.052	0.138	0.137
0–0 S(7)	7199	5.510	0.511	0.513
0–0 S(6)	5833	6.107	0.210	0.201
0–0 S(5)	4587	6.908	0.763	0.656
0–0 S(4)	3476	8.023	0.287	0.204
0–0 S(3)	2504	9.662	0.855	0.467

3 THE MODEL

We solve numerically the hydrodynamic equations on a Cartesian geometry with the direction of the sheared jet allowed to precess and the velocity to pulsate. Material is injected from central zones on the left of the grid. Several jet input parameters are held constant: density, average speed, sound speed, radius, molecular fraction and carbon and oxygen abundances. The jet is initialized with a hydrogenic nucleon density of 10^5 cm^{-3}. We set the jet-to-ambient density ratio to 10, the initial jet temperature to 100 K and the ratio of jet-to-ambient thermal pressure to 100. The nominal, mean axial jet speed is $v_j = 100$ km s^{-1}. This yields an initial Mach number with respect to (the uniform) ambient medium of 140. The media are taken as initially fully molecular with an additional 10 per cent by number of helium atoms, giving the mean atomic mass of 2.32 $\times 10^{-24}$ g. The dust temperature is fixed at 20 K.

The subset of simulations analysed here is summarized in Table 2. Models of slowly precessing jets, with (Q10) and essentially without (R10) pulsation, were described in detail by Smith & Rosen (2005) where CO maps, velocity channel images and position–velocity diagrams were also presented. These had a precession angle of 10°. In contrast, Run P20, providing the signatures of fast precession and a wide precession angle of 20°, was presented by Rosen & Smith (2004a). With basically no precession (A1, which we think of as

Table 2. Major dynamical differences between the input parameters of the presented simulations.

Run	Q10	P20	A1	R10
Precession period	400	50	50	400
Precession angle	10°	20°	1°	10°
Pulsation period	60	60	60	60
Pulse amplitude (per cent)	30	30	30	0.01
Radial shear (per cent)	70	70	80	70

our standard case), a highly focused outflow develops, as explored by Rosen & Smith (2004b). Light molecular jets displayed similar molecular hydrogen structures (Rosen & Smith 2004b) and are not studied here.

We modify the jet velocity in A1, P20 and Q10 with a 30 per cent pulsation and a 60-yr period (see Table 2). In addition, all simulations have a radial shear that reduces the jet velocity at the jet edge to 0.7–0.8 v_j. The precession period is 50 yr in P20, but 400 yr in Q10 and R10. The former is relatively slow compared to the dynamical time $R_j/v_j = 5.4$ yr, but fast relative to the flow evolution time of order 500 yr. The slower rate is of the same order as the flow evolution and also our x-axis crossing time.

The numerical calculations were performed with a modified version of ZEUS-3D (Smith & Rosen 2003), which tracks the molecular fraction, calculates a detailed cooling function, and includes molecular thermal dissociation and reformation on dust grains. The cooling and chemistry are solved implicitly. The computational volume is simulated with a uniform staggered grid divided into zones each of which spans 2×10^{14} cm in each direction. For all the $10°$ precession simulations, we use a grid of $480 \times 205 \times 205$ zones. For model A1 we chose $1000 \times 100 \times 100$, and for model P20, $355 \times 230 \times 230$. The jet radius, R_j, is 1.7×10^{15} cm and is therefore resolved by 8.5 zones. The boundary zones satisfy outflow conditions with the exception of the zones on the inner x-boundary that allow jet inflow.

The H_2 emission line fluxes were calculated as described in detail by Suttner et al. (1997). The population of each vibrational H_2 level was determined through a statistical balance of collisional excitation, de-excitation and radiation. The distribution within a rotational level was approximated by local thermodynamic equilibrium, which should provide a reasonable estimate, although the fluxes of lines originating from the higher rotational states are likely to be under-
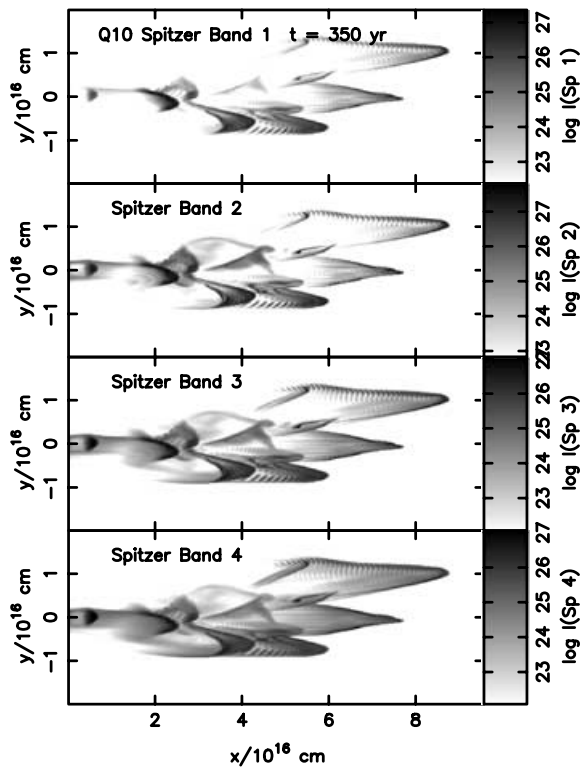
estimated. We also assume that the outflow and foreground cloud are optically thin.

4 THE SYNTHETIC *SPITZER* IMAGES

A slowly precessing pulsating jet produces a sequence of bow shocks visible in all the *Spitzer* bands, as shown in Fig. 2. In band 1, however, only the bow apices would be normally detectable because the grey-scale images display a wide range in surface brightness.

A cavity is swept out by the momentum and transverse expansion, shown on density cross-cuts and millimetre CO images (Smith & Rosen 2005). We could expect that bands 3 and 4 should also display a sign of this cavity through emission from
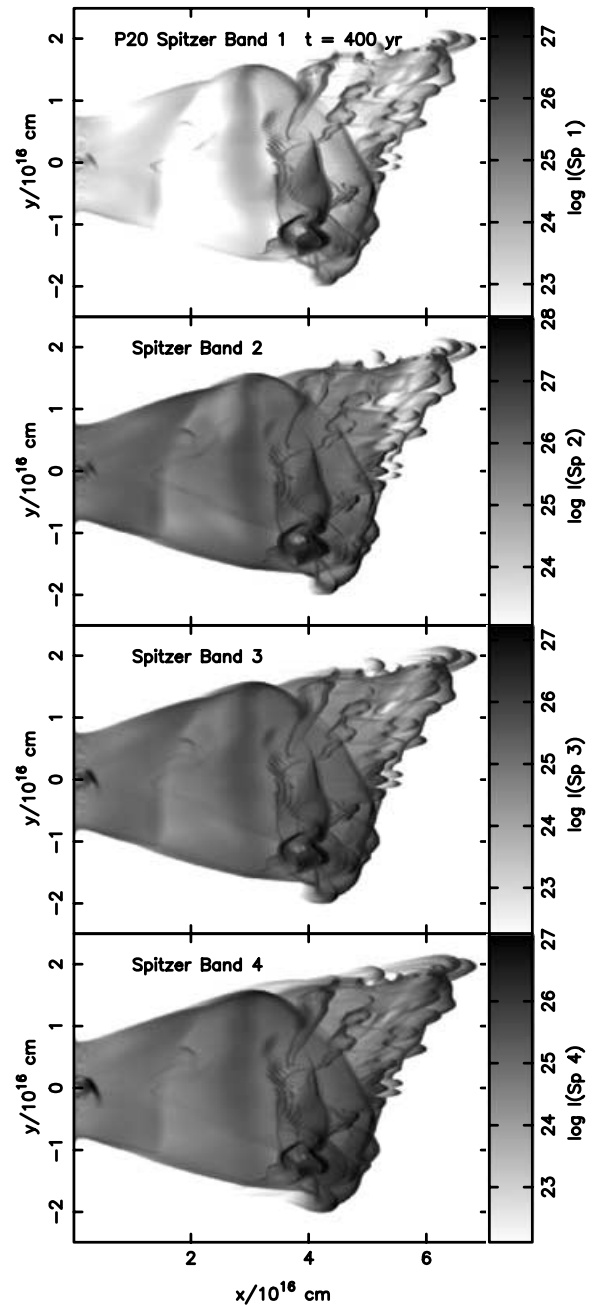
Figure 3. The synthetic images of H_2 emission from the four IRAC bands derived from a simulation of a rapidly precessing and pulsating jet (model P20).

Figure 2. The synthetic images of H_2 emission from the four IRAC bands derived from a numerical simulation of a slow precessing and pulsating jet (model Q10).

low-lying rotational levels of H_2 from the cavity walls. However, evidence for a limb-brightened structure is not apparent in any of the bands. Instead, bands 3 and 4 display long extensions to the flanks of individual bow shocks with little difference which band is chosen.

The inner jet becomes more conspicuous with increasing wavelength. In particular, the inner bow-shaped knot appears wider in band 4. This suggests that these internal jet shocks are of low speed and weak in comparison to the major impact regions where the broken-up jet interacts with the environment.
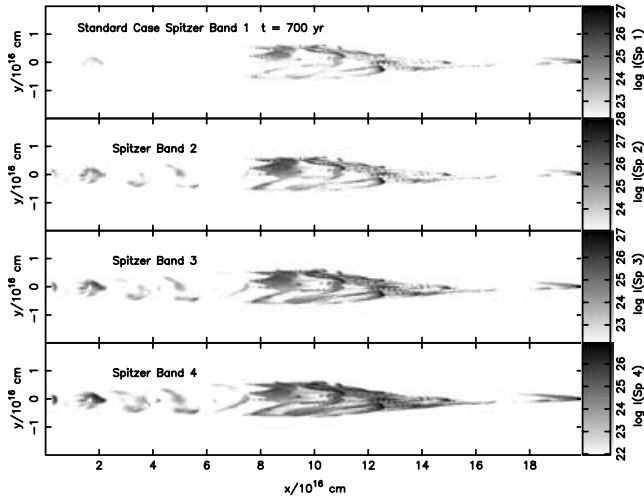
Figure 4. The synthetic images of H_2 emission from the four IRAC bands derived from a simulation of a well-collimated pulsating jet (model A1).
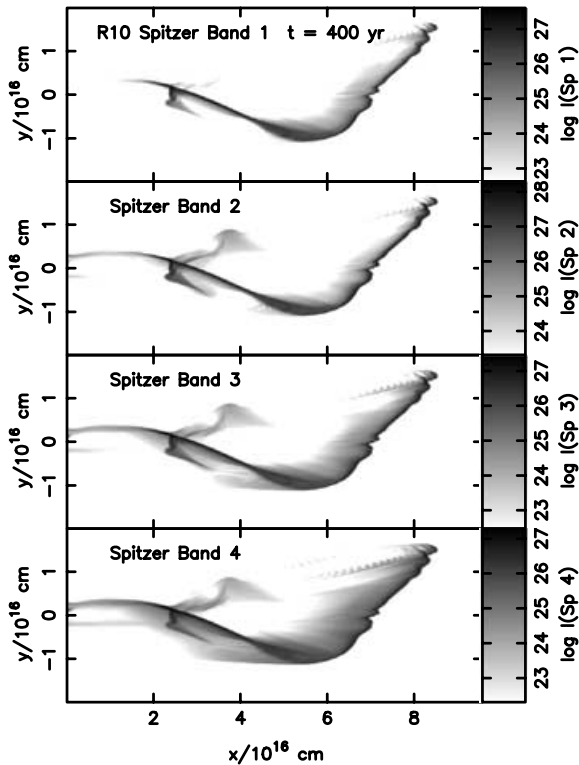

Figure 5. The synthetic images of H_2 emission from the four IRAC bands derived from a simulation of a uniform-speed slowly precessing jet (model R10).

A fast precessing jet excites the cavity walls which become visible in the *Spitzer* bands, as shown in Fig. 3. The brightness is not uniform along the wall. Moreover, diffuse bands of emission and some sharp filaments stretch across the outflow in all bands as a result of the fast precession. Note that the surface brightness of this emission is quite low, at most a few per cent of the peak brightness. The leading ring-shaped interaction region has already fragmented into many small bow shocks. The full extent of these bows is seen in bands 3 and 4, while bands 1 and 2 display much brighter emission from the lower half where the jet is presently interacting with the ambient medium.

Also note the emission from the lower leading edge, which appears to extend outside the cone of emission expected from the precession, apparently a result of the unstable ring and a vortex being shed from the turbulent flow thus created. Finally, the inner jet displays an oblique structure in band 4, which corresponds to a section of the helical shock expected to be generated by the fast precession.

A highly collimated outflow (A1/standard case) results when there is little precession. The jet flow becomes refocused at oblique
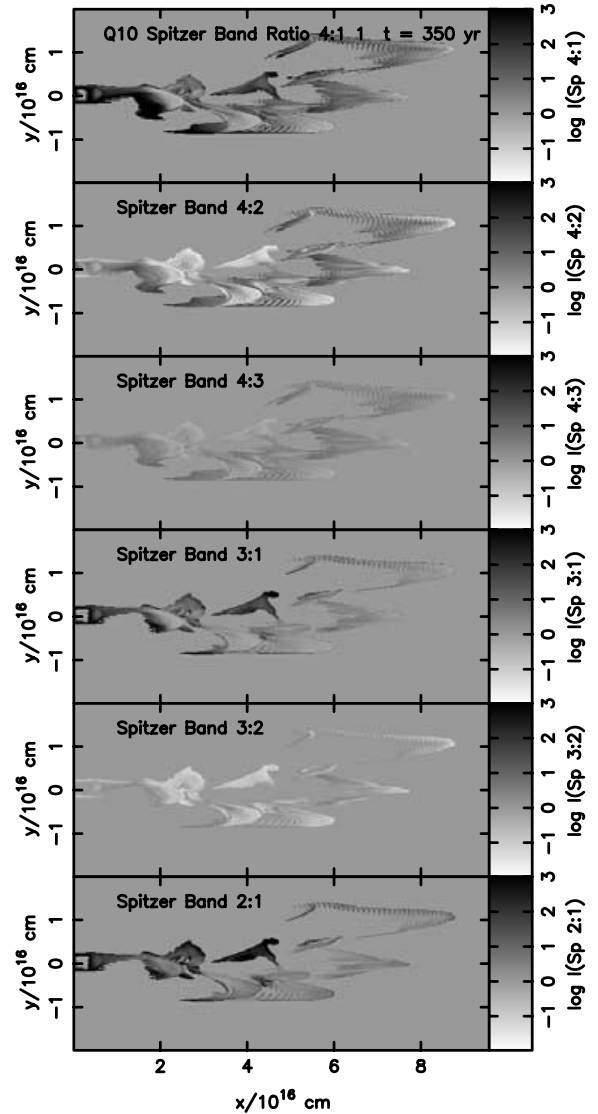

Figure 6. Band ratio images of H_2 emission from the four IRAC bands derived from a numerical simulation of a slow precessing and pulsating jet.

Table 3. The integrated H_2 luminosities of the presented simulations at the times indicated in the band 1 image panels in units of erg s^{-1}.

Run	Band 1	Band 2	Band 3	Band 4
Q10	4.38×10^{29}	2.23×10^{30}	4.73×10^{29}	4.87×10^{29}
P20	1.16×10^{30}	1.25×10^{31}	2.04×10^{30}	1.80×10^{30}
A1	1.00×10^{29}	1.35×10^{30}	2.81×10^{29}	2.98×10^{29}
R10	6.52×10^{29}	4.26×10^{30}	6.61×10^{29}	5.59×10^{29}

shoulders which are prominent H_2 regions roughly mid-way down the outflow. In the IRAC bands (Fig. 4), the H_2 emission covers the shoulders and almost the entire outflow can be traced in band 4.

In the absence of pulsation but with significant precession, the impact region is a continuous roughly helical streamer which is decelerated as it advances into the external medium. As shown in Fig. 5, the streamer is disconnected from the source in band 1 but the connection becomes stronger with increasing wavelength. Apart from this, the differences are rather minor.

The integrated band luminosities from the four simulations are presented in Table 3. Band 2 stands out as the most luminous in all cases. However, this is mainly due to the much lower sensitivity of the detector in bands 3 and 4 (see Fig. 1). Bands 3 and 4 are equally luminous while band 1 is the weakest by a small margin. Given the values tabulated for Cep E, the relatively low flux from band 1 may be partly due to the quite low ambient density, which indicates that local thermodynamic equilibrium is not reached.

Simulation P20 is the brightest outflow in all bands. The reason is that the wide precession distributes the bulk kinetic energy over a wide angle, which is then efficiently dissipated close to the source. In contrast, A1 is the least luminous, consistent with its efficient

transfer of bulk kinetic energy to large distances. Simulation A1 also contains the least 'excited' H_2, i.e. band 4 is relatively strong. In contrast, simulation R10 possesses the highest excitation, probably due to the absence of fragmentation into bow shocks (and because bow shocks tend to be the most aerodynamic with cool oblique wings).

5 IMAGE AND SPECTRAL ANALYSIS

Employing false colours, infrared images are often superimposed to emphasize the structural differences. Here, we present sequences of superimposed images, displaying the ratio of intensities.

Fig. 6 displays the set of six 'band ratio' images for the slow precession and pulsating simulation. Note that a criterion must be employed to construct the ratio maps in order to eliminate regions of low intensity. We take a minimum of 10^{24} erg s^{-1} per zone in the longer wavelength band before the ratio is plotted.

This confirms that comparisons between certain bands do not yield much variation (e.g. 4:3 and 3:2 images). Ratios with band 1 display the most interesting structure. Even the 2:1 image shows large variations. Fig. 7 displays the band ratio images for the outflow driven by a wide precessing jet. Here, large-scale structural variations are apparent. Note that these are again mostly in the panels which contain information from band 1. One exception is the patch of emission from the top right-hand part of the flow, which remains relatively weak and is particularly prominent in all images not containing band 1 information, implying low temperatures.

We have convolved our images with a Gaussian beam with $\sigma = 1.8 \times 10^{15}$ cm. The IRAC pixel scale is 1.2 arcsec. At a source distance of 130 pc (corresponding to the Tauri and ρ Ophiuchi star
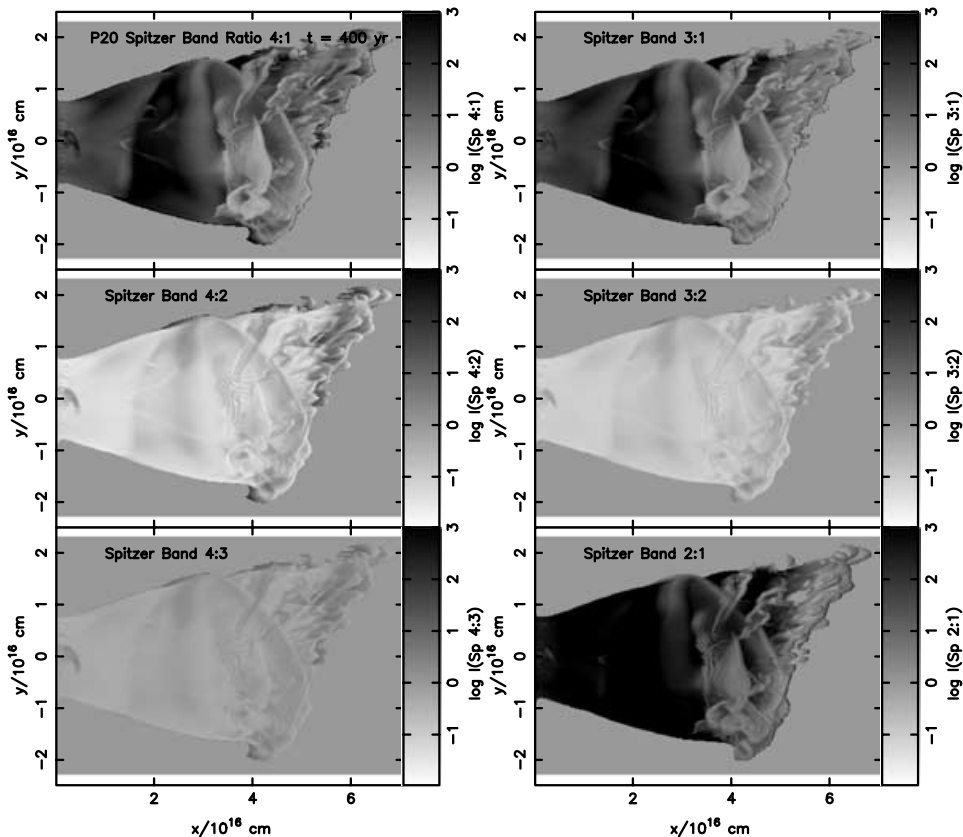

Figure 7. Band ratio images of H_2 emission from the four IRAC bands derived from a numerical simulation of a fast, wide precessing jet (model P20).
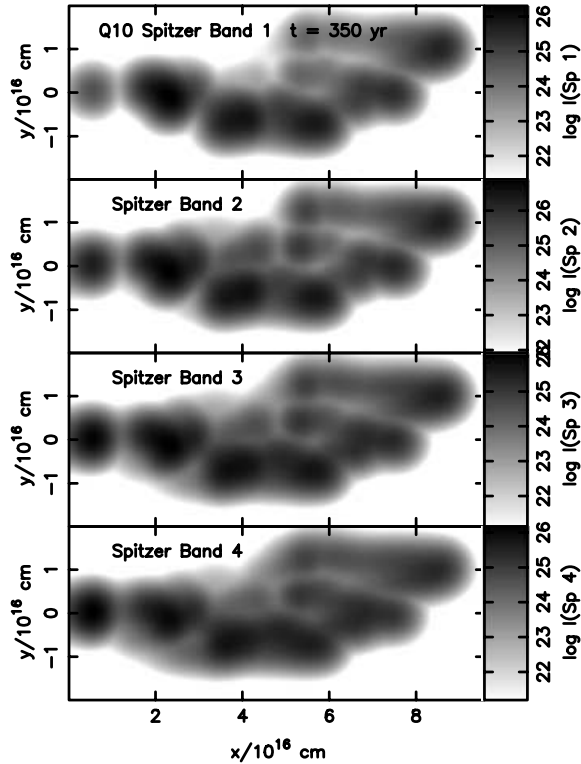
Figure 8. Convolved images of H_2 emission from the four IRAC bands using a Gaussian beam with $\sigma = 1.8 \times 10^{15}$ cm, derived from a numerical simulation of a slow precessing and pulsating jet (model Q10).

formation regions), our standard deviation corresponds to 3/4 pixel, thus corresponding to a point spread function (PSF) with FWHM of roughly 1.5 pixel. This is a reasonable approximation for the present study, but it should be noted that some PSF variations have been measured between the bands (please consult the *Spitzer* Science Centre).

The convolved image displayed in Fig. 8 shows that little detail remains. The bows are diffuse blobs of emission with broad structureless tails. This is indeed the structure that has been observed in Cep E (Noriega-Crespo et al. 2004b). However, in Cep E, emission from bands 2 and 3 appears to extend ahead that of band 1 (i.e. further away from the driving source). This effect is not reproduced in our detailed or convolved images, although we have not attempted to model a specific source when performing the small range of three-dimensional simulations. The individual bows in the wide precessing jet are fully smeared out by the beam (Fig. 9). Note that some helical structure is detectable on the convolved image (e.g. in band 2).

6 DISCUSSION AND CONCLUSIONS

We have calculated the contributions of individual molecular hydrogen lines to the fluxes expected at near-infrared to mid-infrared wavelengths from the bands chosen for the *Spitzer* IRAC instrument. The predictions for steady-state models investigated here were taken from detailed fits to the near-infrared spectra of Cep E. Predictions for time-dependent global properties assumed a hydrodynamic outflow into a uniform medium.

We find that the flux from band 1 is dominated by emission from vibrationally excited H_2 lines with higher mean excitation energy than observed in the K band. The result is that quite sharp features
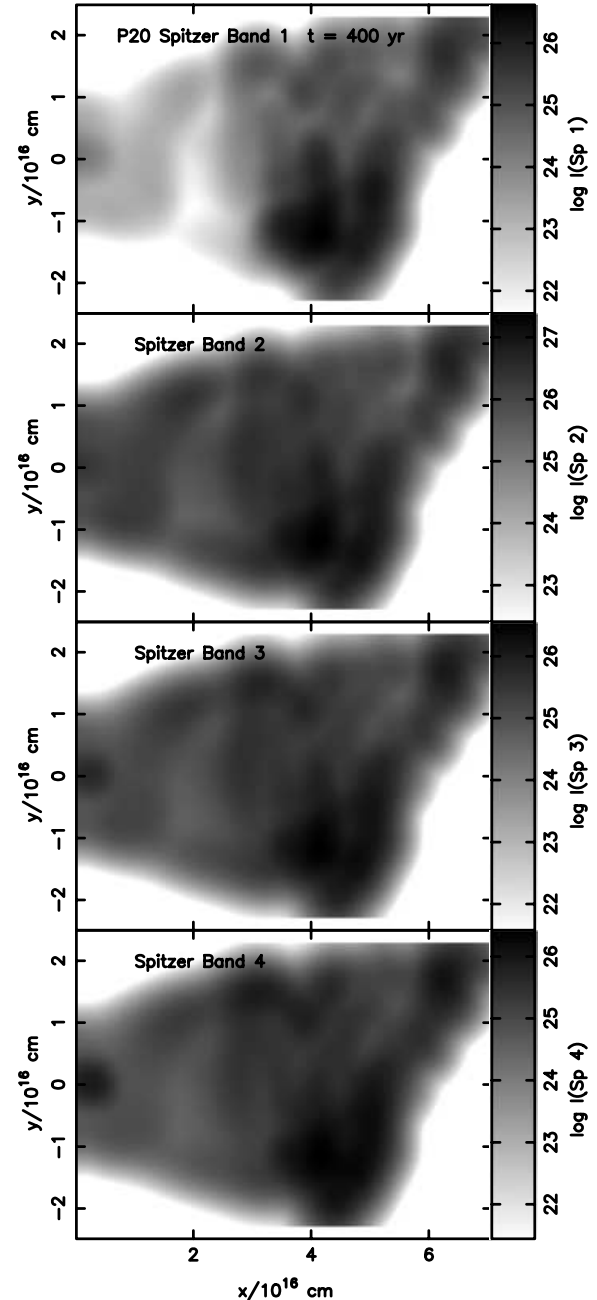

Figure 9. Convolved images of H_2 emission from the four IRAC bands using a Gaussian beam with $\sigma = 1.8 \times 10^{15}$ cm, derived from a numerical simulation of the wide precessing jet (model P20).

are produced, such as arcuate regions from the vicinity of apices of bow shocks.

In bands 2–4, a sequence of broader and longer structures is produced with increasing wavelength. Structure within jets, especially at their base, become relatively brighter and bow flanks become more prominent. However, while these differences are significant, they are not spectacular.

As expected, a well-collimated jet (run A1) generates collimated outflows with relatively weak *Spitzer* fluxes. The most dissipative mid-infrared outflow in all bands corresponds to the fast precessing jet (run P20).

In the simulations and the steady-state model, the strongest integrated H_2 emission is predicted to arise from band 2, although this

is mainly due to the higher spectral response. The 0–0 O(9) and 0–0 O(11) make the dominant contributions, while the strongest intrinsic emission arises from 0–0 O(5).

The only simulated outflow which produces some cavity wall structure in H_2 IRAC bands was found to be driven by a wide precessing jet. This confirms the finding of Raga et al. (2004) that cavity walls capable of interpreting the HH46/47 outflow require a precessing jet. However, we find that the cavity wall is not strongly limb brightened. This could suggest that the global structure produced by a hydrodynamic flow may be valid but the shock physics may be inaccurate for HH46/47. It should also be noted that cavity shapes depend on the physics, especially the total cooling (Blondin, Fryxell & Konigl 1990), which leads to atomic flows being significantly more conical and molecular flows much more tubular (Rosen & Smith 2004b).

Alternative physics that could aid in understanding the observed flows include ambipolar diffusion and C-type shocks. Such shocks yield a higher fraction of the overall energy budget as infrared emission. However, a higher shock speed would be necessary to raise the excitation of the magnetically cushioned shock. It is not clear how higher speeds may arise at the cavity walls without the global shape of the outflow being altered. Instead, with the insight provided by these simulations all driven by jets of $100 \, \text{km s}^{-1}$, jets propagating at higher speeds through the ambient medium should generate higher speed transverse shocks into the cloud and raise the excitation in the cavity walls.

The molecular hydrogen simulations presented here provide a fundamental basis for comparison. However, only by performing simulations and presenting the equivalent images for other configurations may we eliminate some options. The structure associated with magnetohydrodynamics models, wind models, atomic jets and non-uniform environments are just some of the possibilities. Jet speed, density and extinction may also considerably alter what we measure.

ACKNOWLEDGMENTS

REFERENCES

Blondin J. M., Fryxell B. A., Konigl A., 1990, ApJ, 360, 370
Davis C. J., 2002, RevMexAA Conf. Ser., 13, 36
McGroarty F., Ray T. P., Bally J., 2004, A&A, 415, 189
Noriega-Crespo A. et al., 2004a, ApJS, 154, 352
Noriega-Crespo A., Moro-Martin A., Carey S., Morris P. W., Padgett D. L., Latter W. B., Muzerolle J., 2004b, ApJS, 154, 402
Raga A. C., Noriega-Crespo A., González R. F., Velázquez P. F., 2004, ApJS, 154, 346
Reipurth B., Bally J., 2001, ARA&A, 39, 403
Richer J. S., Shepherd D. S., Cabrit S., Bachiller R., Churchwell E., 2000, in Mannings V., Boss A. P., Russell, S. S., eds, Protostars and Planets IV. Univ. of Arizona Press, Tuscon, p. 867
Rosen A., Smith M. D., 2004a, MNRAS, 347, 1097
Rosen A., Smith M. D., 2004b, A&A, 413, 593
Smith M. D., Rosen A., 2003, MNRAS, 339, 133
Smith M. D., Rosen A., 2005, MNRAS, in press
Smith M. D., Eisloffel J., Davis C. J., 1998, MNRAS, 297, 687
Smith M. D., Froebrich D., Eislöffel J., 2003, ApJ, 592, 245
Suttner G., Smith M. D., Yorke H. W., Zinnecker H., 1997, A&A, 318, 595

This paper has been typeset from a TEX/LATEX file prepared by the author.